Inorganic Chemistry

Article

pubs.acs.org/IC

$La_{10}W_2O_{21}$: An Anion-Deficient Fluorite-Related Superstructure with Oxide Ion Conduction

Marie-Hélène Chambrier,*,[†] Armel Le Bail,[‡] Fabien Giovannelli,[§] Abdelkrim Redjaïmia,[∥] Pierre Florian,[⊥] Dominique Massiot,[⊥] Emmanuelle Suard,[#] and François Goutenoire[‡]

[†]Unité de Catalyse et de Chimie du Solide, UMR-CNRS 8181, Université d'Artois, Rue Jean Souvraz, 62300 Lens, France

[‡]Institut des Molécules et des Matériaux du Mans, Département Oxydes et Fluorures , UMR-CNRS 6283, Université du Maine, 72085 Le Mans Cedex 9, France

[§]Groupe de Recherche en Matériaux, Microélectronique, Acoustique et Nanotechnologies, UMR-CNRS 7347, Université F. Rabelais, CS 2903, 41029 Blois Cedex, France

[∥]Université de Lorraine, Institut Jean Lamour, UMR-CNRS 7198, Ecole des Mines de Nancy, Parc de Saurupt, CS 14 234, 54042 Nancy Cedex, France

[⊥]Condition Extrême et Matériaux: Haute Température et Irradiation, CNRS-UPR 3079, 1d Avenue de la Recherche Scientifique, 45071 Orléans Cedex 2, France

[#]Institut Laue Langevin, Avenue des Martyrs, B. P. 156, 38042 Grenoble Cedex, France

Ⓢ *Supporting Information*

ABSTRACT: The crystal structure of $La_{10}W_2O_{21}$, which has to be reformulated $(La_{5.667}W_{0.333})LaWO_{14}\square_2$, is best described, on average, by a 2 × 2 × 2 anion-deficient fluorite-related superstructure cubic cell, with space group $F\bar{4}3m$, $Z = 4$, and $a = 11.17932(6)$ Å, similar to $Y_7ReO_{14-\delta}$. The 32 cations are distributed with lanthanum on the 4a-site, tungsten on the 4b-site, and a partial occupancy of the 24g-site by La (94%) and W. The 56 oxygen atoms occupy four 16e-sites, three of them fully and with an occupancy of 1/2 for the fourth one. Others $M_{10}W_2O_{21}$ (M = Er, Y) adopt a 3 × 2 × 2 fluorite superstructure with W in octahedral sites, whereas W is mainly in tetrahedral sites in $La_{10}W_2O_{21}$. Several powerful techniques such as crystal image furnace synthesis, ^{139}La nuclear magnetic resonance (NMR) and convergent beam electron diffraction (CBED) were used to achieve our results. Transmission electron microscopy (microdiffraction, CBED, and Tanaka patterns) brought us the real symmetry, showing that indeed classical cubic twinning along the 3-fold axis does take place. The surprising La/W mixed site is nicely confirmed by ^{139}La NMR. This compound exhibits interesting fast oxide ion conducting properties, comparable with LAMOX (Lacorre et al. *Nature* **2000**, *404*, 856−858) at low temperature. As opposed to many ionic conductors, no temperature structural transition is observed. Its conductivity is about 6.4 × 10^{-4} S·cm^{-1} at 700 °C.

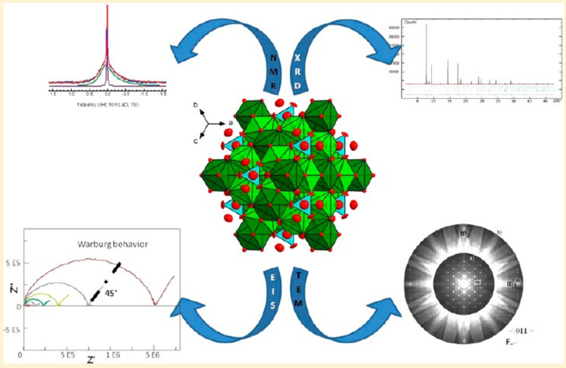

■ INTRODUCTION

Fuel cells are a potential alternative to fossil fuels in order to reduce environmental impact. Many technologies could be employed: proton exchange membrane fuel cell (PEMFC), phosphoric acid fuel cell (PAFC), molten carbonate fuel cell (MCFC), alkaline fuel cell (AFC), and solid oxide fuel cell (SOFC). In the field of the SOFC, the solid electrolyte should present a high ionic conduction, but also a high chemical stability, a negligible electronic conduction, and good mechanical properties. The compounds which present such high ionic conduction by O^{2-} are rather rare, mainly due to the fact that O^{2-} species present a large ionic radius in comparison with the other atoms in the structure. Until recently, these interesting materials were belonging to only a small family with a particular composition of great structural groups such as the fluorite type (stabilized zirconia,[2] δ-Bi_2O_3,[3] scheelite[4]) or perovskites ($LaGaO_3$,[5,6] $Ba_2In_2O_5$[7]), intergrowth Bi_2O_2 layer/perovkite (BIMEVOX[8]), and pyrochlore.[9] Over the past few years, new structural types have integrated this very small class of compounds: apatite $La_{9.33}SiO_{26}$[10] and LAMOX $La_2Mo_2O_9$.[1]

The research of such new materials is rather difficult. Of course, the mobility of such a big O^{2-} anion is not common. Nevertheless, some guidelines[11] and analysis of the known compounds could give some general rules in order to find such a new material. We can bring to light four points: (1) there is need for a large number of mobile species and also (2) a large number of empty sites; (3) the empty and occupied sites should have similar potential energies with a low activation energy barrier; and finally (4) the cation framework should be

Received: July 12, 2013
Published: December 10, 2013

highly polarizable. The presence of empty sites is not always a strict condition. The last series of high ionic conductors are made of two distinct families: the one with empty sites named anionic vacancy and the other one with interstitial oxygen.

Noticeable examples of the first family, oxides with anionic vacancies, are the stabilized zirconia $Zr_{1-x}Y_xO_{2-\delta}$ (for $x = 0.08$ and $\delta = 0.04$) and the perovskite $LaGaO_3$ doped ($La_{0.9}Sr_{0.1}Ga_{0.8}Mg_{0.2}O_{3-\delta}$). The Brownmillerite $Ba_2In_2O_5$ could also be regarded as a structure with anionic vacancies due to its relation with the perovskite structure. Indeed, the tetrahedral environment of the indium atom replaces the usual octahedral coordination of the B cation in the ABO_3 perovskite.

The second family is more restricted because of the difficulty of proving or justifying the existence of such interstitial oxygen atoms. In the scheelite structural type $Pb_{1-x}La_xO_{4+\delta}$, the authors[4] have used simple density measurement (pycnometry) to demonstrate the presence of extra oxygens. With the more recently discovered oxide ion conductor $La_{9.33}\square_{0.66}Si_6O_{26}$,[12] it seems that the conductivity could be improved with a small oxygen excess and cationic vacancy leading to the general formula $La_9SrSi_6O_{26.5}$.[12] Nevertheless, it is generally really difficult to observe such extra oxygen.

It is important to mention that not only the electronic charge balance should be observed but also the intrinsic volume of the big atom. In ionic compounds such as oxides, the large ionic radii atoms are mainly the oxygens. In common oxides, the volume per anion ranges between 18 and 22 Å^3, if we consider the usual ionic radii of an oxygen atom, $r(O^{2-}) = 1.40$ Å.[13] Of course such very simple consideration will give spurious result in the case of big cations and does not take into account the covalent character of some bonds.

West[11] has pointed out the effect of the polarizability of the cations. It is interesting to notice that the most recent oxide ion conductors systematically present a big cation with high polarizability factor such as Ba^{2+}, La^{3+}, Bi^{3+}, and Pb^{2+}.

Hereafter, we present a new lanthanum-containing compound with interesting oxide ion conduction based on anionic vacancies. This definite compound $La_{10}W_2O_{21}$ has been known for 40 years,[14] but the crystal structure and the conduction property were not clearly identified. A lot of confusion was made with the La_6WO_{12} composition. Indeed, at least five phase diagrams were built in the 1970s and *are* different on many points, namely, on the $La_{10}W_2O_{21}$ existence. In this work, we will refer to Yoshimura and Rouanet's phase diagram (Figure 1).

The same formula is also mentioned in many other Ln_2O_3–MoO_3 (Ln = Gd, Nd)[15,16] phase diagrams. In previous works, $Ln_{10}(Mo/W)_2O_{21}$ were always mentioned as a pyrochlore-related structure with cubic cell parameter $a = 11.167$ Å for $La_{10}W_2O_{21}$, except for Er and Y[17] which present an orthorhombic fluorine superstructure with cell parameters $3a_{\text{fluorine}}$, $2a_{\text{fluorine}}$, and $2a_{\text{fluorine}}$. Nevertheless, no structural analysis was performed, and this assumption was derived only from the analysis of the cell parameters. The pyrochlore structural type is related to the mineral pyrochlore $(Ca,Na)_2Nb_2O_6(O,OH,F)$ but atopites $(Ca,Mn,Na)_2Sb_2(O,OH,F)_7$[18] also described this large family. The pyrochlore structure is usually described as $A_2B_2O_6O'$ or $A_2B_2X_7$.[19] Analysis of the cell parameters given by Wyckoff[18] ranges from 9.89 Å for the mineral ralstonite to 10.699 Å for $Zr_2Ce_2O_7$. With more recent data obtained from the Inorganic Crystal Structure Database (ICSD), the maximum cell parameter is found for Bi_2LaTaO_7 ($a = 10.96$ Å),[20] Bi_2InNbO_7 ($a = 10.79$ Å).[21]

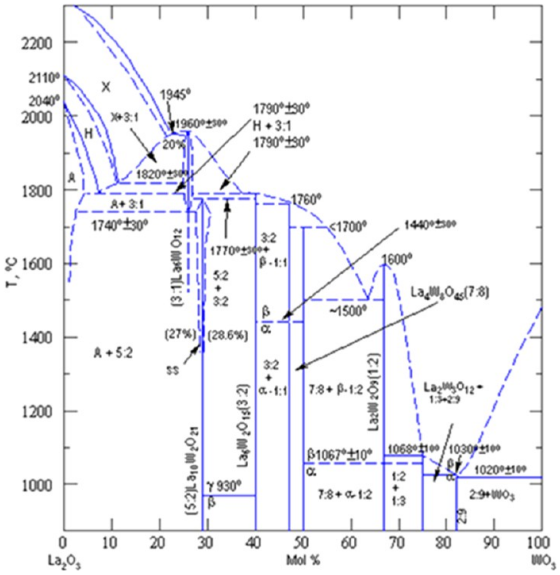

Figure 1. La_2O_3–WO_3 phase diagram from Yoshimura and Rouanet's work. Reprinted with permission from ref 14. Copyright 1976 Elsevier.

More recently, Haugsrud and Kjolseth[22] have studied the La_6WO_{12} proton conductivity, and Magraso et al.[23] have determined its structure. These reliable results are deeply serious but do not take into consideration that the La_6WO_{12} definite compound is not stable at temperatures lower than 1740 °C, as indicated in the La_2O_3–WO_3 phase diagram.[14] Historically, a lot of confusion has occurred between these two definite compounds due to their numerous structural similarities and the difficulties encountered with their synthesis.

The aim of this study is to elucidate the "$La_{10}W_2O_{21}$" structure in order to understand and give a first explanation of the ionic conductivity property.

■ EXPERIMENTAL SECTION

Lanthanum oxide powder was dried and decarbonated at 1000 °C overnight prior to use. The starting oxides La_2O_3 and WO_3 (Riedel-de Haën, 99%) were weighted in stoichiometric proportions, depending on the wanted molar ratio (from 22 to 32% WO_3) and ground together in an agate mortar. The prepared composition was then heated at 1550 °C for one night in an alumina crucible, with no particular condition being used in order to cool the sample. The X-ray measurements were performed on a small amount (~0.5 g) of the compound. For the neutron diffraction experiments, a larger amount sample (28.7 mol % WO_3) was prepared (~15 g). The final compound was white.

The X-ray diffractograms were in good agreement with the expected $La_{10}W_2O_{21}$ (28.7 mol % WO_3) previously studied by Yoshimura and Rouanet[14] with the JCPDF reference 00-030-0687.

High-intensity and high-resolution synchrotron powder diffraction data were collected on a Debye–Scherrer diffractometer, BM01A, instrument at ESRF, Grenoble, France. Measurements were done at room temperature, on a 0.3 mm capillary using a wavelength $\lambda = 0.60044$ Å over 1– 65° 2θ with an increment step of 0.003° for a total counting time of ~3 h.

High-temperature X-ray diffractograms were acquired on a Bragg–Brentano diffractometer (MPD-PRO Panalytical) with copper radiation equipped with a linear detector X'Celerator and an Anton Paar HTK12 furnace. The high-temperature X-ray diffraction patterns were collected during one night, from 5 to 70° (2θ), for 25, 1100 °C (by steps of 100 °C). Neutron diffraction data were collected on the powder diffractometer D2B instrument at ILL, Grenoble, France. Data collections were performed at constant wavelength $\lambda \sim 1.59398(4)$ Å on ~15 g of compressed powder of 28.7 mol % WO_3 compound and at room temperature. For the pattern, the increment step was 0.05° (2θ), the interval of data collection ranging from 0 to 162°, and the total counting time was ~2 h with a high flux and medium resolution configuration.

The density measurement was performed on a gas picnometer ACCUPIC 1330 (Micromeritics) with helium gas and using approximately 2 g of sample. The temperature of measurement was 24 ± 1 °C.

In order to obtain a single crystal, calcined powders (28.7 mol % WO_3) were compacted in 5 mm diameter latex tubes and isostatically pressed under 4000 bar. The resulting rods were then sintered in alumina plates at 1550 °C for 48 h in order to obtain long, straight, and dense feed rods which are critical parameters for subsequent crystal growth. The crystal growth experiment was handled using an optical floating zone furnace (Cyberstar) equipped with two 1000 W halogen lamps placed in semiellipsoidal mirrors and focusing onto one point. The sintered feed rod is hanging in the upper part of the furnace and aligned with the seed rod, fixed at the bottom part. To start the experiment, the power of the lamp is gradually increased until the tip of the feed rod is melting. Another sintering rod was fixed in the lower part of the furnace, and brought into contact with the molten zone. The floating zone melt growth parameters were kept as follows: ambient air; growth rate, 5 mm/h. A rotation speed of 20 rpm was applied on both rods in opposite direction in order to get a homogeneous molten zone in shape and in composition.

The nuclear magnetic resonance (NMR) spectrum was acquired on a 17.6 T Bruker Avance II spectrometer operating at a ^{139}La frequency of 106.0 MHz with a magic angle spinning Bruker probehead using 4 mm diameter zirconia rotors. The experiment was carried out under static conditions, using a Hahn echo sequence with central-transition-selective $\pi/2$ pulses of 1.0 μs (corresponding to a radio frequency field rf = 30 kHz), echo delay of 100 μs to ensure the acquisition of the full echo,[24] a recycle delay of 250 ms, and a spectral width of 1.67 MHz. The spectrum is broader than the excitation bandwidth of the radio frequency pulse and was hence obtained with the variable offset cumulative spectrum (VOCS) technique,[25,26] which consists of acquiring subspectra at different irradiation frequency's offsets and summing them to reconstruct the broadband spectrum. Offset's steps of 50 kHz were used, leading to 27 subspectra with 1000 transients acquired for each of them. ^{139}La chemical shifts were referenced to a 1 M solution of $LaCl_3$ at 0 ppm. After removing the constant-offset baseline arising from the presence of the external transitions, the spectrum was simulated using a modified version of the DMFit program.[27]

The electron diffraction study was performed on a 200 kV side entry JEOL2010 transmission electron microscope with a double-tilt specimen holder operating at room temperature. Convergent beam electron diffraction (CBED) and Tanaka patterns were obtained with a CM12 Philips transmission electron microscope operated at 120 KV.

The sample was prepared by grinding a small amount of powder in an agate mortar and pestle under dry 1-butanol to produce a suspension. A drop of the suspension was deposited on a holey carbon film supported by a 1000 mesh copper grid and dried.

The ionic conductivity measurements were performed by complex impedance spectroscopy in the 10 MHz to 1 Hz frequency range with an applied voltage of 100 mV using a Solartron SI 1260 impedance gain-phase analyzer with Smart[28] impedance software for data acquisition. The data were acquired on pellets of 5 mm diameter and 4 mm thickness, with platinum electrodes deposited under a vacuum on both faces. Impedance data were obtained in the 100−700 °C temperature range under N_2. The sample was allowed to equilibrate for 30 min at each temperature prior to data acquisition, in order to ensure thermodynamic equilibrium. The total conductivity was obtained from the resistance value provided from the intersection between the half-circle and the Z' axis on the Nyquist plot.

Structural Investigation. The main difficulty of this work arose at the beginning of the structural investigation. Indeed, search-matching through the ICDD poweder diffraction file (ICDD-PDF) using the EVA (Bruker) software was positive but suggested a quasi-identity between $La_{10}W_2O_{21}$ and La_6WO_{12} (PDF 30-0686); the latter crystallizes in a face centered cubic system with lattice parameter a = 11.179 Å.[29] However, Yoshimura et al.[29] stated that La_6WO_{12} *"has a C-type bcc symmetry, and that it is stable only at high temperatures (above 1740 °C). Below this temperature, it changes into the* $La_{10}W_2O_{21}$ *phase (+*La_2O_3*) which they announced to have a pyrochlore-like fcc symmetry."* It points out the difficulty in determining the border between the two definite compounds $La_{10}W_2O_{21}$ (28.6% WO_3) and La_6WO_{12} (25% WO_3). Indeed, less than 3% WO_3 split up these two definite compounds which justifies the confusion encountered in the several phase diagrams established. From these issues many questions arose: Is the La_6WO_{12} compound stable at room temperature? Does a solid solution between $La_{10}W_2O_{21}$ and La_6WO_{12} really not exist?

In order to best comprehend, several syntheses (see Experimental Section) were made by varying the WO_3 molar percent between 20 and 32%. At WO_3 molar percent smaller than 28%, the obtained compound reacts rapidly with air moisture. After differential thermal analysis (DTA) and thermogravimetric analysis (TGA), we have evidenced the presence of La_2O_3 which evolves to form $La(OH)_3$. Quickly at higher WO_3 contents, the lower form of $La_6W_2O_{15}$ appears (Figure 2). This compound was easily recognizable by DTA due to its two phase transitions (630 and 930 °C). Indeed it presents three polymorphic forms α, β, and γ. So, as mentioned by previous works dealing with the phase diagram, $La_6W_2O_{15}$ may not belong to a solid solution domain (Figure 2). From that, we were sure of a definite compound existence around 28 mol % WO_3 mentioned as $La_{10}W_2O_{21}$ and the inexistence of solid solution between this definite compound and La_6WO_{12}

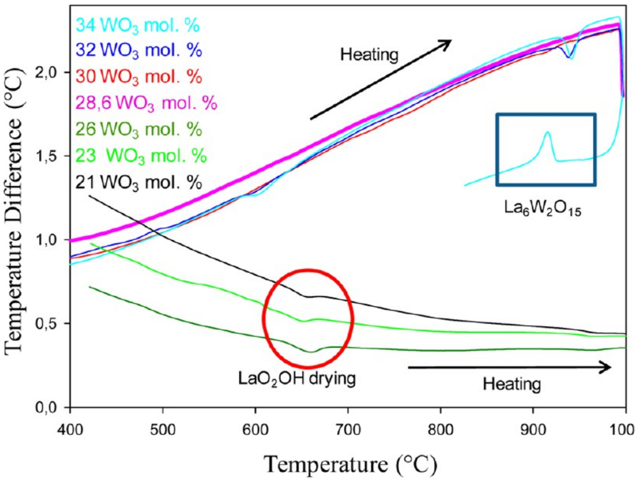

Figure 2. Differential scanning calorimetry analysis of the compound series between 21 and 34 mol % WO_3, showing an endothermic peak corresponding to dehydration of LaO_2OH while heating the compound at 21, 23, and 26 mol % WO_3 and showing the $\gamma \to \beta$ $La_6W_2O_{15}$ phase transition while heating the compound at 30, 32, and 34 mol % WO_3.

With these clues, it was now interesting to focus on the $La_{10}W_2O_{21}$ crystallography, which was supposed to be related to the pyrochlore structure in Yoshimura's works. Rationally, our first attempt was done in this direction. To begin, we can note that pyrochlore structure crystallizes in the space group $Fd\bar{3}\ m$ (no. 227) with the following general reflection conditions: hkl, same parity; $h00$, $h = 4n$. The peak (200) is then usually absent, as opposed to our study where it appears at 16.11° (2θ). This peak rules out the last reflection condition, and the general conditions hkl with the same parity have to be considered, leading to five possible space groups: $F2_3$ (no. 196), $Fm\bar{3}$ (no. 202), $F4_32$ (no. 209), $F\bar{4}_3m$ (no. 226), and $Fm\bar{3}\ m$ (no. 225). A second analysis in the ICSD data leads to a relatively large number of pyrochlores in the $F\bar{4}3m$ (no. 216) space group. We used the compound $Bi_{1.6}Y_{0.4}Sn_2O_7$[30] as the structural model.

In order to match the structural model with the formula of $La_{10}W_2O_{21}$, the following structural analysis was performed. $Bi_{1.6}Y_{0.4}Sn_2O_7$ has a cell parameter of a = 10.61 Å with Z = 8. So the atomic content, in the cubic cell, is $A_{16}B_{16}X_{56}$. In order to match this composition we have to take Z = 2.66 for $La_{10}W_2O_{21}$, which gives the formulation $La_{26.66}W_{5.32}O_{55.95}$. To actually confirm Z, a density measurement was done; the result 6.50(9) g/cm^3 is close to the calculated density of 6.60 g/cm^3 for Z = 2.66.

The Rietveld refinement on the X-ray diffraction data leads to a correct solution (Table 1). The atomic distances and the bond valence calculation are rather good. The bond valence calculation for La1 leads to a small value (2.50(1)) in comparison with the true oxidation state +3. For the mixed site La/W the value is on the contrary slightly in excess at 4.44(3) compared to the expected [(+3) × 0.66] + [(+6) × 0.33] = +4. The bond valence calculations for all oxygen atoms are very close to the expected value of −2. Some small peaks appear in the X-ray diffraction data, showing the presence of additional phases (La_2O_3 or $La_6W_2O_{15}$). As mentioned previously in this phase diagram, it does not present a solid solution domain and it is always difficult to obtain really pure compounds.

Table 1. Summary of the Different Rietveld Refinements from High-Resolution Neutron Pattern in Different Subgroups of $Fd\bar{3}m$ (No. 227)

space group	no.	$\sim R_{Bragg}$ (%)	comments
$Fd\bar{3}m$	227	17	impossible due to (200) peak
$F_4\bar{3}m$	216	15	B iso
$I4_1/amd$	141	17	a = 7.89 Å, c = 11.17 Å, FD problem
$R\bar{3}m$	*166*	*11.7*	
$I\bar{4}m2$	*119*	*12*	
$I4_12_2$	98	17.1	FD problem
$I4_1/a$	88	17.6	
$I\bar{4}_2d$	122	18	
$R\bar{3}$	148	13.5	
$R3m$	160	40	complicated model
$R3_2$	155	17	
$Imma$	*74*	*11.7*	
$C2/m$	12		impossible due to (200) peak

In order to have a better analysis of the oxygen positions powder neutron diffraction patterns have been recorded at the D2B (ILL) line. The first pattern was recorded in 2H with high-flux setting (low resolution) on a powder sample. A second pattern was recorded in one night with high resolution on a different sample. The refinement of the structural model obtained from the X-ray powder pattern with the first (low-resolution) neutron pattern did not lead to a satisfactory result: R_{Bragg} = 14.6%; R_{wp} = 20.9% . Different structural models with the same space group (no. 216) were tested with isotropic or anisotropic thermal agitation factor without improving the results.

A modulation is easily observed in the background of the neutron diffraction pattern (Figure 3). This modulation is similar to the one we observed for $La_2Mo_2O_9$[1] in the same conditions. Such a modulation of the background is usually due to diffuse scattering coming from local static structural disorder.[31] The Debye formula can be used to express the contribution of static structural disorder in diffuse elastic scattering.[32] It exhibits a first marked maximum for Q_{max}= (2π × 1.23)/d_m, where d_m is the preferred pair distances. As in $La_2Mo_2O_9$, the maximum 2θ angle corresponds to Q_{max} = 3.1 Å^{-1}, which gives a preferred pair distance around 2.5 Å. This last distance could be characteristic of the shortest oxygen−oxygen distances.

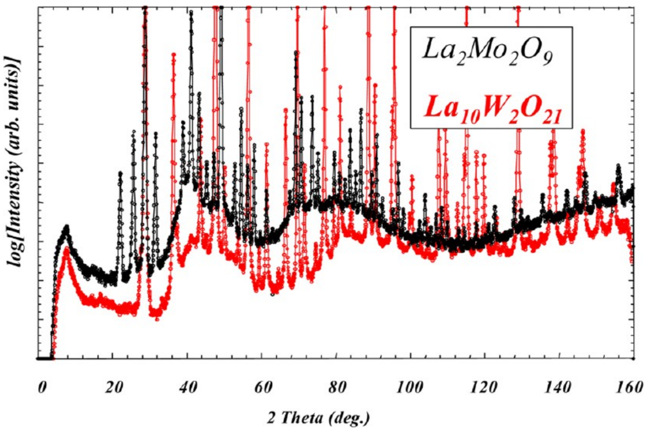

Figure 3. Details of the background for $La_2Mo_2O_9$ and for $La_{10}W_2O_{21}$ for the neutron powder diffraction. The large diffuse peak observed around 46° (2θ) corresponds to 3.1 Å^{-1}. Such a value is due to short-range order with a distance of 2.5 Å, a sign of the oxygen disorder.

The ^{139}La NMR spectrum shown on Figure 4 does not display the set of sharp discontinuities expected for a crystalline material found in the—very scarce—^{139}La NMR literature detailing work performed on inorganic oxides[33−37] and suggests that some disorder is present in the material. The broad asymmetric line ranging from 0.5 to 1.0 kHz spans a frequency range comparable with the one observed for La_2O_3[35] and hence can be attributed to the effect of the electric field gradient (EFG) on the lanthanum site which produces quadrupolar broadening on the ^{139}La NMR line shape. When compared to La_2O_3, this frequency range points to a nuclear quadrupolar coupling constant C_Q on the order of 60 MHz and the absence of discontinuities to the fact that there is a distribution of EFGs at the lanthanum sites. A second, much sharper, line is located around 0 kHz, evidencing the existence of a site with a very small C_Q, i.e., with a local environment being close to spherically symmetric. This type of two-component spectra has been previously observed in LaNa−Y zeolites[36] and has been ascribed to hydrated lanthanum ions in the large cavities (sharp line) and lanthanum cations in the sodalite cages (broad line).

The EFG distribution can be handled using the approach originally developed by Czjzek et al.,[38] further formulated into a general model for the distribution of electric field gradients in disordered solids by Le Caër et al.[39] and implemented along with a distribution of isotropic chemical shift in our laboratory developed simulation software DmFit.[40] This leads to the very satisfactory two-component fit displayed on the right side of Figure 3. The sharp line is found to be a Gaussian line characterized by a position of 134.9 ppm and a width of 21.3 kHz, and the Czjzek-based simulation of the other line leads to an isotropic chemical shift of δ_{iso} = 767 ppm and a mean quadrupolar coupling constant C_Q = 70.3 MHz. This latter broad component accounts for 86% of the total integrated intensity.

A word of caution must nevertheless be put with this two-site simulation. Recently, the Czjzek model has been extended and successfully applied to ^{71}Ga static NMR line shapes in chalcogenide glasses.[41] Some of the computed spectra obtained in this study display striking similarities with the one we obtained here and are based on a sole environment. If it is clear that the computed sharp discontinuity is misplaced with respect to the position of the Gaussian line obtained for our compound and hence that we do not favor such a single-site decomposition, we cannot completely rule out the possibility of a peculiar EFG distribution (i.e., distribution of structural parameters) applied on a single crystallographic site and which would lead to our observed spectra.

A systematic full width at half-maximum (fwhm) analysis has been done for $La_{10}W_2O_{21}$ powder from neutron and X-ray diffraction data. To begin, a comparison is made between fwhm obtained for powder $La_{10}W_2O_{21}$ and those obtained for a referenced sample (NAC; the diffraction pattern was collected in the same conditions; Figure 5a). We see an important difference: $La_{10}W_2O_{21}$ peak widths are twice those of the NAC compound. To continue, we focalized on the η value at high diffraction angle. The peaks shapes obtained from the peak fitting routines implemented in Winplotr[42] and using a pseudo-Voigt peak shape pointed out large values for some *klh* family peaks. It is related to an important Lorentzian contribution. The same

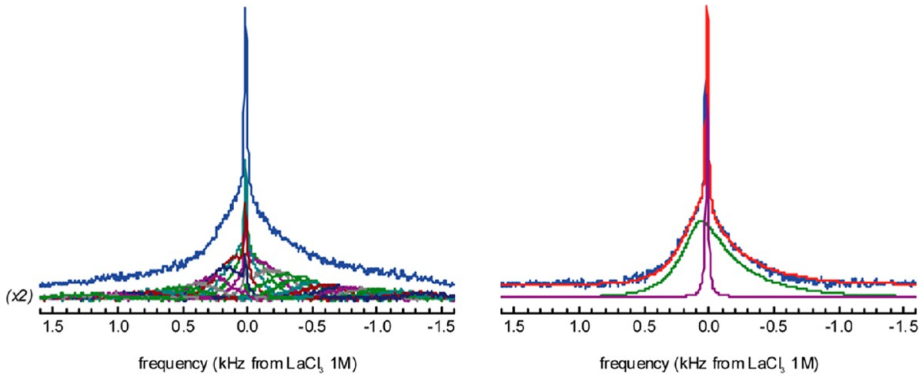

Figure 4. ^{139}La NMR spectra of $La_{10}W_2O_{21}$. On the left is shown the experimental spectrum reconstructed from the sum of the (magnified) individual components displayed below the spectrum (VOCS procedure; see text for details) and on the right the simulation along with the two individual components.

conclusions are deduced from X-ray diffraction data. So, peak width and shape analysis highlight strong microstructural anomalies (default, disorder, and distortions, ...). In order to obtain a single crystal for structural analysis, some tests were done in an image furnace on cylindrical rods (5 mm diameter; 25−30 mm length). Our attempts to syntheszes $La_{10}W_2O_{21}$ single crystals led to the correct composition, but all tested crystals were systematically twinned and could hence not be used. Several crystals were nevertheless crushed, and their X-ray powder diffraction pattern displayed systematically strong Lorentzian peak shapes and even sometimes hyper-Lorentzian peak shapes. Those peak shapes are compared with LaB_6 recorded in the same conditions (Figure 5b). La_2WO_6 fwhm values are also shown and present more or less the same values as those of reference compound LaB_6, so we could deduce $La_{10}W_2O_{21}$ fwhm values are due only to microstructural effects and not to the chemical system La_2O_3−WO_3.

The pyrochore structural type is known to present many different distortions. The unusual diffraction peak shapes observed from X-ray laboratory and neutron patterns suggested the possibility of small distortions. In order to investigate such distortions, we have used the subgroups of the usual pyrochlore structure. Selected area electron diffraction analyses were performed. On most of the crystals analyzed, thin reflections are observed with no evidence of extra diffraction reflections (Figure 6). As no extra reflections implying the increase of the a cell parameter of the cubic cell could be evidenced, we focused our work on subgroups simply deduced from the $Fd\bar{3}m$ space group. Such study was done with the help of the Isodisplacive program.[43] Thirteen space groups were tested, considering only quadratic, rhomboedric, and orthorhombic subgroups plus one monoclinic space group. The high-resolution neutron powder pattern was used for such analysis. In a first step, the structural model deduced by the program Isodisplacive was used with isotropic thermal agitation. Then Fourier difference maps were calculated in order to check for residual nuclear density with the help of the program Gfou implemented in Winplotr.[44] In some space groups, the Fourier difference maps led to more negative maxima than positive maxima, and those Fourier maps were then considered as problematic. Otherwise, the positive residual nuclear density was considered as a new atomic position. Following this procedure, one space group has given a better reliability factor $R\bar{3}m$, with $R_{Bragg} \sim 11.7\%$, than the original structure. Attempts using anisotropic thermal agitation or a new atomic position from Fourier difference have failed.

The medium quality of the powder refinement suggests it would be valuable to re-explore the composition of the compound. In the phase diagram proposed by Yoshimura and Rouanet,[14] a high-temperature form of La_6WO_{12} is mentioned. This compound is believed to a have a cubic structure with $a = 11.17$ Å with similar PDF file. The chemical composition of the two phases are close for $La_{10}W_2O_{21}$: it is $2/(2 + 5) = 28.7$ mol % in WO_3 and for La_6WO_{12} $1/(1 + 3) = 25$ mol %. At 40 mol % WO_3, the $La_6W_2O_{15}$ composition appeared. This compound shows two phase transitions at 630 and 930 °C. By the analysis of these two phase transitions for different compositions in the range of 25−35 mol %, it is possible to have access to its composition through the analysis of the Tammann curve. We have also used the analysis of the intensity ratio of the different compounds: La_2O_3 I_{max} at 30.5° 2θ, $La_{10}W_2O_{21}$ I_{max} at 27.7° 2θ, and $La_6W_2O_{15}$ I_{max} at 29.2° 2θ. This method is of course spoiled by the peaks overlap, but it can still give some reliable chemical compositions. Both methods favored the 28,7 mol % composition with respect to the 25 mol % one (Figure 7).

Transmission Electron Microscopy. Selected area electron diffraction was performed. Thin reflections were observed indicating that the compound was well-crystallized (Figure 6). ED patterns were indexed in a cubic lattice with cell parameter $a \approx 11.2$ Å. Tilting crystals along different reciprocal lattice directions revealed the existence of the hkl conditions: $h + k$, $h + l$, and $k + l = 2n$ (Figure 6), consistent with a face-centered lattice, this ED pattern corresponds to the [001] zone axis.

In addition, we note that strong and weak reflections were simultaneously present; considering intense reflections only, a subcell with the new parameter $c' = c/2 \approx 5.5$ Å was obtained.

In the recent past decades, CBED[45,46] has been adopted for the identification of unknown phases. This technique reveals three-dimensional (3-D) symmetry information, which enables rapid determination of crystallographic structure (point and space groups). The CBED whole pattern (WP) is composed of transmitted and diffracted disks, grouped in ZOLZ (zero-order Laue zone) and FOLZ (first-order Laue zone). Specimens containing very fine crystals and/or defected crystal give relatively poor CBED patterns, showing little or no intensity variation within the disks. As a result, crystallographic identification becomes difficult and even sometimes impossible. An alternative technique, the microdiffraction, can alleviate those limitations.[47,48] With this method, the disk diameter in the CBED pattern is reduced by using a nearly parallel electron beam, thereby improving the angular resolution and reducing the diffuse scattering in the diffraction pattern. By considering both, "net symmetry" (position of reflection) and "ideal symmetry" (position and intensity of reflections) of the ZOLZ and of the WP (ZOLZ + FOLZ), one can identify the point and space groups of the crystal. The same notation and terms are used in the present paper as the systematic procedure proposed by Morniroli et al.[47,48] to derive the point and space groups of crystal.

The first step was to identify the crystal system, and the highest net symmetries observed for this phase are 4*mm* (Figure 8a) and 6*mm* (Figure 8b), which, according to Table 7 in ref 47, corresponds to a cubic system. Both 4*mm* and 6*mm* symmetries are respectively recorded along ⟨001⟩ and ⟨111⟩ zones axes, as indicated in Table 2 in ref 47.

The second step was the resolution of the Bravais lattice and glide plane from the extinction symbol found. The specific symmetrical zone axes patterns (ZAPs) required for Bravais lattice and glide plane identifications are ⟨001⟩ and ⟨110⟩ (Table 5 in ref 47). The comparison between the nets of the zero-order and first-order Laue zones, in particular the comparison of the periodicity and the shift

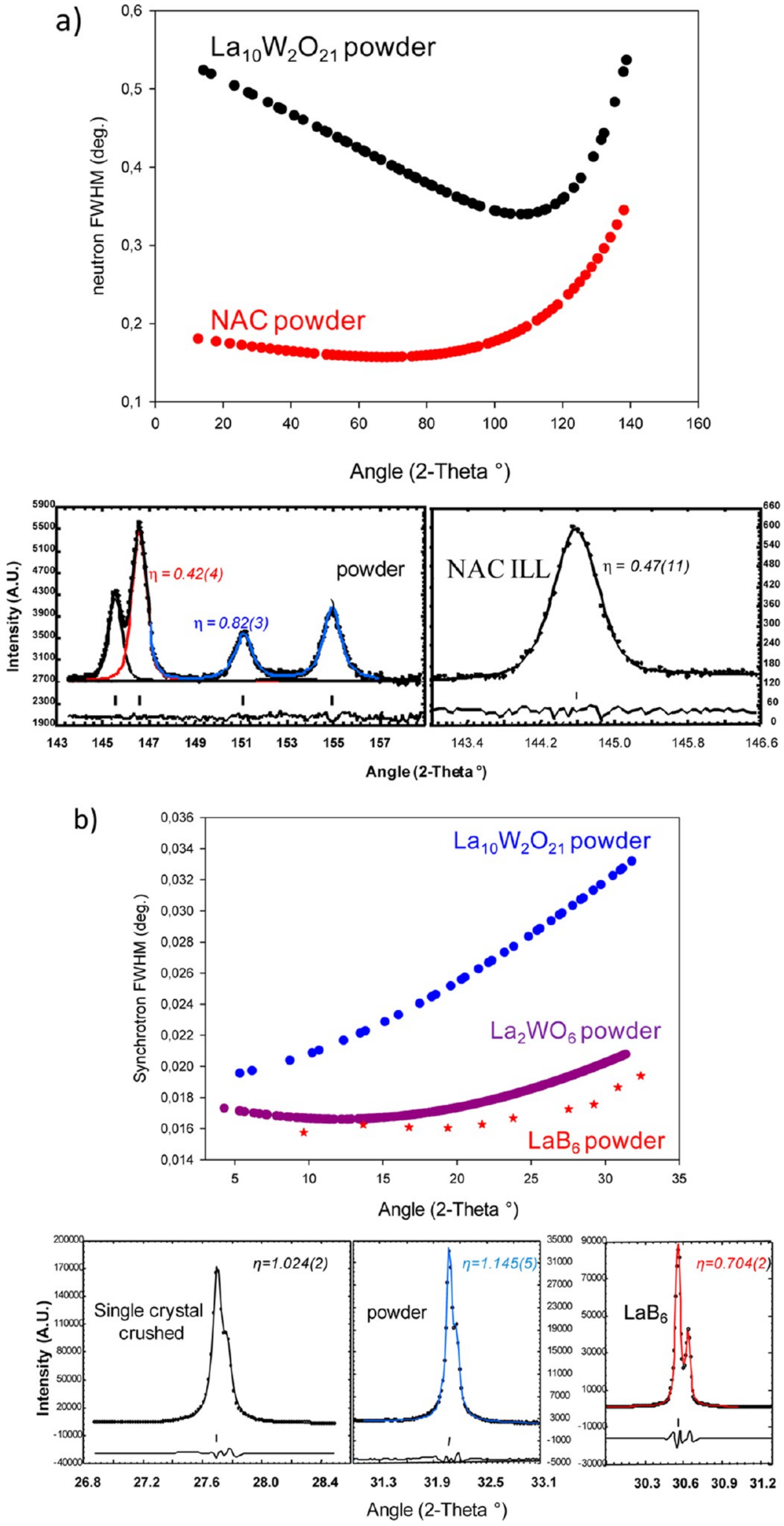

Figure 5. Profile analysis (fwhm and η) of diffraction peaks from neutron (a) and X-rays diffraction (b) patterns from $La_{10}W_2O_{21}$ powder and crushed single crystal. The fwhm evolution with angle 2θ is compared with reference compounds (NAC for neutron and LaB_6 for synchrotron) measured in the same conditions in a similar 2θ range. For the synchrotron case, a comparison is also done with another compound from the $La_2O_3-WO_3$ phase diagram: La_2WO_6.

between the two zones, leads to individual extinction symbols for every ZAP. The combination of the individual extinction symbol gives a partial extinction symbol, which, in accordance with ref 47, leads to one or a limited number of space groups.

Unfortunately, the reflections in the FOLZ are not visible on the ⟨001⟩ symmetrical pattern (Figure 8a). They can be observed by tilting the specimen slightly around the zone axis until FOLZ areas appear on the pattern (Figure 9a).

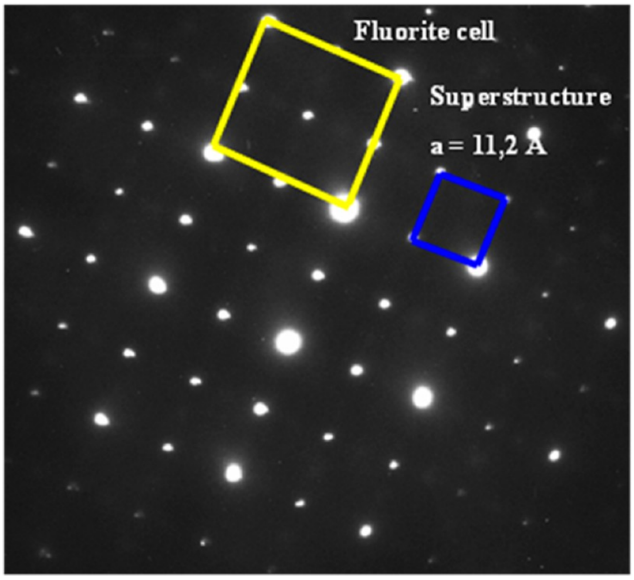

Figure 6. Electron diffraction pattern of $La_{10}W_2O_{21}$ along [100]*. The fluorite superstructure is enhanced.

On the $\langle 001 \rangle$ tilted ZAP, two perpendicular mirrors m_1 and m_2 are identified. The smallest squares, drawn in the ZOLZ and in the FOLZ, have their sides parallel to the m_1 and m_2 mirrors. The squares are identical and half-shifted along the two mirrors. The same periodicity and the half-shift between these two zones lead to the I-.. or F-.. extinction symbols. Therefore, the distinction between the I and F Bravais lattices is not possible from observation of this unique $\langle 001 \rangle$ ZAP. To remove this ambiguity, one must consider the $\langle 110 \rangle$ ZAP.

The $\langle 110 \rangle$ ZAP (Figure 9b) exhibits (2*mm*), 2*mm* net symmetries. Two perpendicular mirrors m_1 and m_2 are identified. The smallest centered rectangles, drawn in the ZOLZ and in the FOLZ, have their sides parallel to the m_1 and m_2 mirrors. The same periodicity and the absence of shift between these two zones leads to the F..- extinction symbol.

The two experimental ZAPs recorded along $\langle 001 \rangle$ and $\langle 110 \rangle$ give the following individual extinction symbols: F-.. and F..-. The addition of these results gives the partial extinction symbol F--- which indicates that there is no glide plane perpendicular to the $\langle 001 \rangle$ or $\langle 110 \rangle$ directions. According to Table 3.2 in ref 47 the partial extinction symbol F--- is in agreement with five space groups associated with five point groups.[49] The possible space groups satisfying such conditions are listed in Table 2.

And the last but not the least step was the identification of the point group and space group. To make the distinction between these five possible space groups, the point group must be identified. This can be obtained from the observation of the $\langle 111 \rangle$ ZAP "ideal" symmetry as indicated in Table 4 in ref 47. This symmetrical $\langle 111 \rangle$ pattern (Figure 7b) exhibits a $(\underline{6mm})$ $\underline{3m}$ ideal symmetry.

According to Table 4 in ref 47 the point group corresponding to $(\underline{6mm})$, $\underline{3m}$ ideal symmetries is $m\bar{3}m$, excluding the other four points groups. It is concluded that the space group of this investigated $La_{10}W_2O_{21}$ phase is $Fm\bar{3}m$ or $F(4/m)\bar{3}(2/m)$, in its full crystallographic notation.

For this phase, it was also possible to determine the $m\bar{3}m$ point group by considering the $\langle 111 \rangle$ Tanaka CBED patterns (Figure 10). This Tanaka CBED pattern is derived from the symmetrical (6 *mm*) $\langle 111 \rangle$ CBED pattern by tilting the specimen until six discs are in the exact Bragg position.[46] The $\langle 111 \rangle$ Tanaka CBED pattern, displaying 2-D symmetry information inside the six discs, leads to the 6 $mm1_R$ projected diffraction group[46] (Table 3). The $6mm1_R$ projected diffraction group is in agreement with five diffraction groups associated with five different point groups and three crystal systems. The possible point groups satisfying such conditions are listed in Table 3.

For the cubic system, the $6mm1_R$ projected diffraction group corresponds to the 6_Rmm_R diffraction group and belongs to the point group of symmetry $m\bar{3}m$.[46] This result corroborates the one obtained by the first method.

Figure 11 shows a montage of electron microdiffraction patterns recorded along the principal zone axes, namely, [001], [110], and [111]. These ZAPs are coherently indexed.

Ab Initio Structure Determination. This study is limited to the characterization of the average structure, because the synchrotron data show the beginning of a slight peak-splitting at large angle, meaning that either the sample is not homogeneous or the symmetry is not cubic. In any case, we have no other possibility than to consider the structure being close to cubic. Cell parameters were easily found from several indexing softwares such as TREOR,[50] DICVOL[51] and McMaille[52] and from transmission electron microscopy in a diffraction way (Figure 7).

We derived from the extinction conditions mentioned above that the probable space group of highest symmetry is $Fm\bar{3}m$ (also possible are $F\bar{4}_3m$, $F4_32$, $Fm\bar{3}$, and $F23$). We do not observe the weak *hkl* reflections 211, 411, and 332 (etc.) listed for La_6WO_{12}, said to be due to a cation ordering during a cooling process of the sample prepared by co-fusion methods. Such space groups are hardly compatible directly with a pyrochlore-like model (ideally $Fd\bar{3}m$), and all attempts to produce such an arrangement failed. After extraction of the intensities[53] by using the FULLPROF software,[54] a convincing model in the $F\bar{4}_3m$ space group was obtained from the neutron diffraction data by using the direct-space ESPOIR software.[55] The cationic distribution was found to reproduce a 2 × 2 × 2 superstructure of the fluorite CaF_2. This model is similar to that established recently from single-crystal data for $Y_7ReO_{14-\delta}$,[56] described in the $Fm\bar{3}m$ space group. However, the $F\bar{4}_3m$ space group allows for more ordering of the oxygen atoms (two oxygen atom 32f-sites in $Fm\bar{3}m$, one fully occupied and the other 3/4 occupied, are split into four 16e-sites in $F\bar{4}_3m$, three fully and one-half occupied) gaining 2% on the reliability factors .This $F\bar{4}_3m$ space group leads to the appearance of WO_4 tetrahedra instead of the ReO_8 cubes found in the yttrium rhenium oxide. Ehrenberg et al.[56] interpret their Re coordination as disordered $[ReO_4]$ tetrahedral, but it may be suggested that microtwinning could have masked the true space group (if really that structure is cubic). The recently determined structure $La_{18}W_{10}O_{57}$[57] was believed previously (Yoshimura) to be "$La_{14}W_8O_{45}$"; we thus first considered possible that the true composition of our compound could have been $La_{14}W_2O_{27}$, as revealed from the structure determination first approach, instead of $La_{10}W_2O_{21}$. However, the sample is prepared from 5:2 La_2O_3:WO_3, and even if La_2O_3 is detected as an impurity for some preparations (see the synchrotron pattern, Figure 12), its presence on the neutron diffraction data (Figure 13) is quite negligible (less negligible is the diffusion in the background, very similar to that observed for $La_2Mo_2O_9$,[1] in accordance with the conduction properties). The thermal parameter for the 24g-site when fully occupied by La atoms was obtained slight too small from the synchrotron data and slightly too large from the neutron data, suggesting that there could be some W−La substitution (0.055% in order to match with the title formula), whereas the 4a- and 4b-sites appear fully occupied by La and W atoms, respectively. According to our results, from a synchrotron−neutron mixed Rietveld refinement (Table 4), the $La_{10}W_2O_{21}$ compound formula, if rewritten as corresponding to an anion-deficient MX_{2-y} fluorite, becomes $(La_{5.67}W_{0.33})LaWO_{14}\square_2$ (Z = 4) or $(La_{0.83}W_{0.17})$-$O_{1.75}$ (y = 0.25) (Table 5 and Figure 14). This idealized description leads to satisfying interatomic distances (Table 6), but neglects to take into account the perturbation of the 0.055% of W atoms on the 24g-site, and this may explain the neutron R_B factor (8.6%) higher than the synchrotron one (4.7%). To account for this discrepancy, one would have to modify the occupancy factors of O1, O2, and O3 and to split their sites, which looks unreasonable in a Rietveld refinement. The other $M_{10}W_2O_{21}$ (M = Er, Y) phases adopt a 3 × 2 × 2 ordered fluorite superstructure with four-fifths of the M atoms being in 7-fold coordination by O, and the remainder being 6-fold-coordinated, while the W cations are in octahedral sites.[16] W is mainly in tetrahedral sites in $La_{10}W_2O_{21}$ (the 4b-site), though the bond valence calculations show

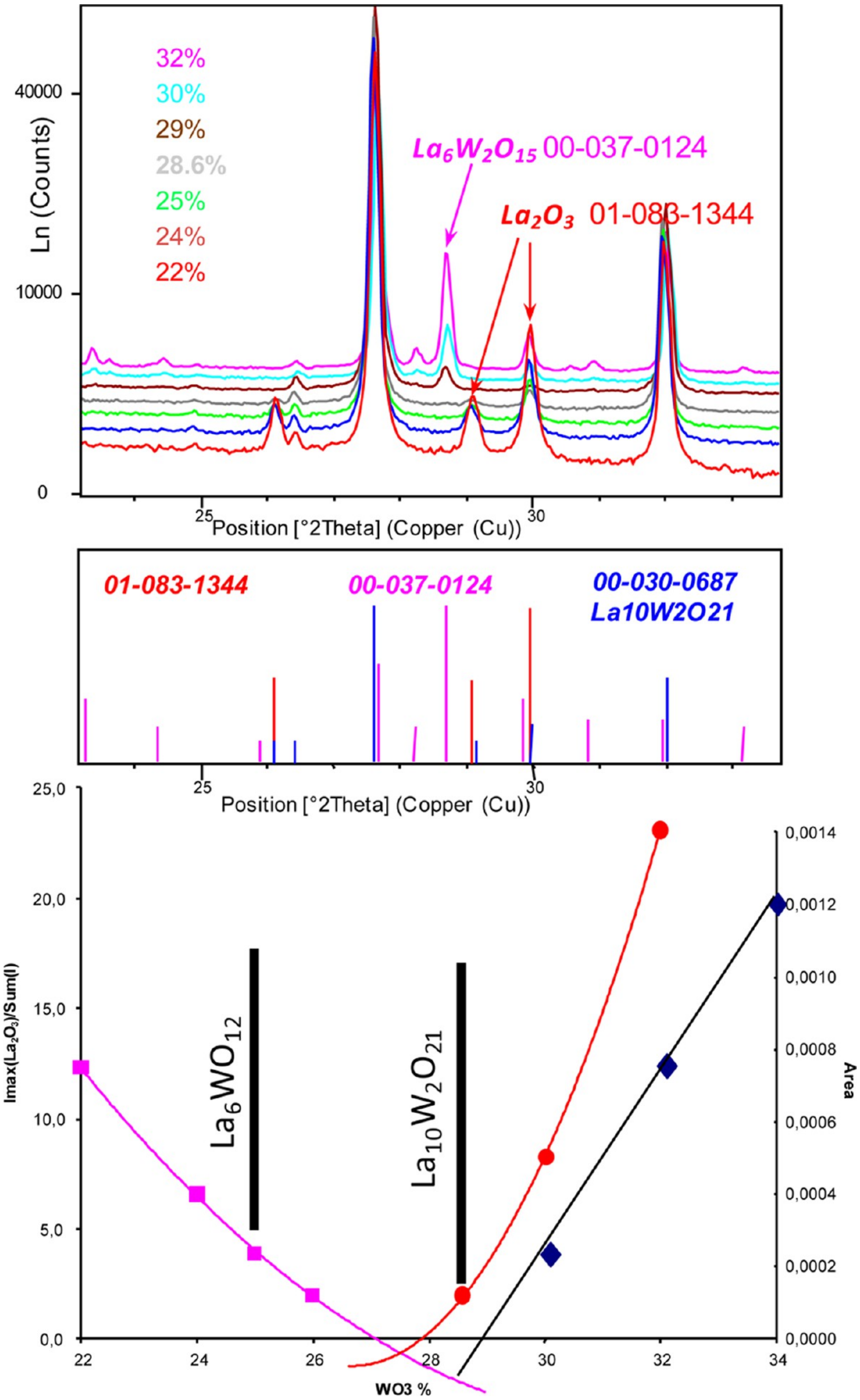

Figure 7. (Top) XRD diffractograms of different compositions from 22 to 32% WO_3. Both impurities, La_2O_3 and $La_6W_2O_{15}$, are observed. (Middle) Different PDF files. (Bottom) Intensity ratios: from $ILa_2O_3/(ILa_{10}W_2O_{21}+ILa_2O_3)$, squares; from $ILa_6W_2O_{15}/(ILa_{10}W_2O_{21}+ILa_6W_2O_{15})$, dots. Lines are plotted as a guide to the eye. The intensity of the $La_6W_2O_{15}$ phase transitions from the b to the a form for 29, 32, and 34% WO_3. It leads to the Tammann plot, the limit composition found for $La_6W_2O_{15}$ is 29%, and this confirms $La_{10}W_2O_{21}$ instead of La_6WO_{12}.

that O4 is needed to attain the expected W^{6+} (Table 7). The majority (85%) of the La atoms are in 7-fold coordination (considering the half-occupation of O4), the remaining (4a-site) being in 8-fold cubic coordination (Figure 14). This agrees with ^{139}La NMR results which found ~15% of La atoms in a high symmetric site and the 85% in a significantly distorted site.

Which atom is moving during conduction and plays a role in the neutron diffusion observed in the background? It is very probably O4, which would jump toward the oxygen vacancies due to the half-occupation of the site, forming an intercrossing system of tunnels parallel to the [110] direction (Figure 15). The distances between O4 and a vacancy are 3.52 and 4.38 Å between two sites bonded to the

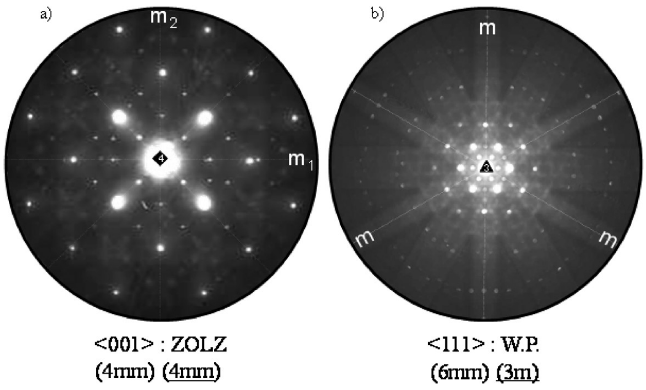

Figure 8. Electron microdiffraction patterns recorded along (a) ⟨001⟩ showing ZOLZ with symmetries 4*mm* and (b) ⟨111⟩ whole patterns with symmetry 3*m*.

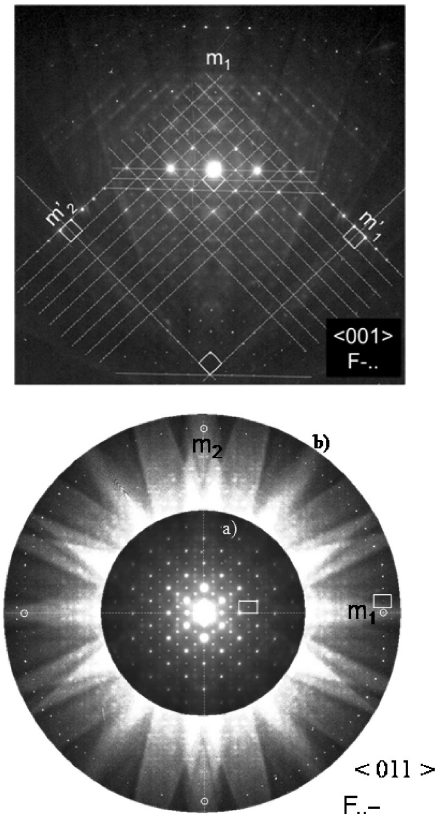

Figure 9. (a) FOLZ electron microdiffraction patterns slightly tilted along ⟨001⟩; (b) ZAP electron microdiffraction patterns along ⟨110⟩ ZAP exhibiting (2*mm*), 2*mm* symmetry.

Table 2. Possible Space Groups Belonging to F--- Extinction Symbol

extinction symbol	space groups	point groups
F---	F_23	23
	$Fm\bar{3}$	$m\bar{3}$
	$F4_32$	432
	$F4_32$	432
	$F\bar{4}_3m$	$\bar{4}3m$
	$Fm\bar{3}m$	$m\bar{3}m$

same W and along the diagonal O(4)−□ of the [La(1)O_7□] polyhedron, respectively.

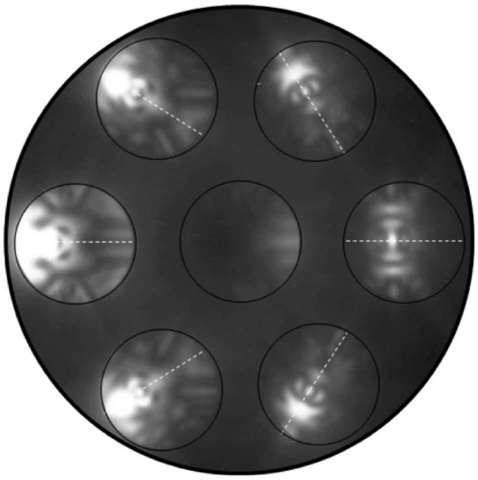

Figure 10. Tanaka CBED patterns along ⟨111⟩ and its six disks in exact Bragg position showing the symmetry 6*mm*.

Table 3. Point and Diffraction Groups Related to the Projected Diffraction Group $6mm1_R$

projected diffraction group			$6mm1_R$		
diffraction groups	$6m_Rm_R$	$6mm$	$6mm1_R$	6_Rmm_R	6_Rmm_R
point groups	622	$6mm$	$6/mmm$	$3m$	$m\bar{3}m$
crystal systems		hexagonal		trigonal	cubic

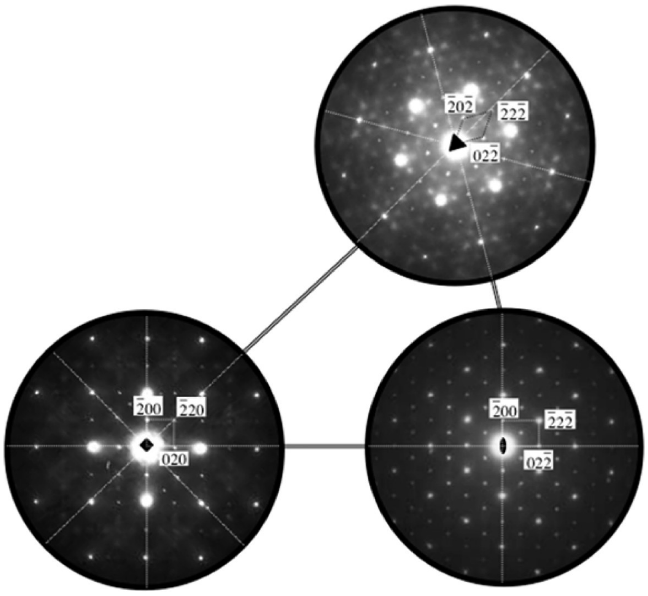

Figure 11. Montage of coherently indexed electron diffraction patterns recorded along the principal zone axes, namely, [001], [110], and [111] of the phase $La_{10}W_2O_{21}$.

Due to the high similarity between the powder patterns of $La_{10}W_2O_{21}$ and quenched La_6WO_{12}, their structure should not differ too much, the latter being slightly more ordered (not F-centered). Moreover, a very limited solid solution $(La_{6-x}W_x)LaWO_{13.5+1.5x}\square_{2.5-1.5x}$ with $x = 1/3 \pm \delta$, and δ very small, cannot be excluded around the $La_{10}W_2O_{21}$ formulation ($x = 1/3$).

Conductivity Measurement and Thermal Expansion. In the same phase diagram La_2O_3−WO_3, the high cubic temperature form of $La_2W_2O_9$[58] has been recently evidenced to have an oxide ionic conduction as good as $La_2Mo_2O_9$. The modulated background observed in the neutron diffraction experiments and the structural

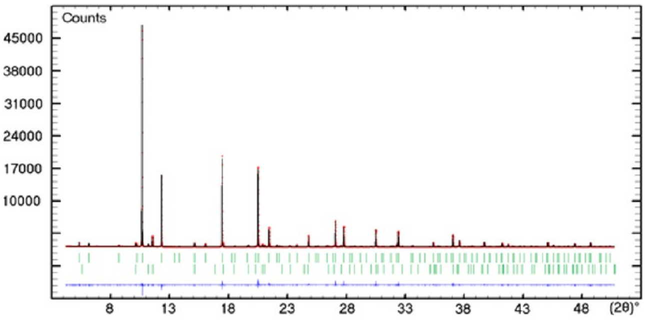

Figure 12. Refined diffraction pattern from synchrotron data for $La_{10}W_2O_{21}$ and the La_2O_3 impurity because the compound is at 28.6 mol % WO_3. Red dots represent the observed data, the black line represents the calculated ones, Bragg ticks are the peak positions, and the blue curve shows the difference between the observed and calculated patterns. λ = 0.60044 Å.

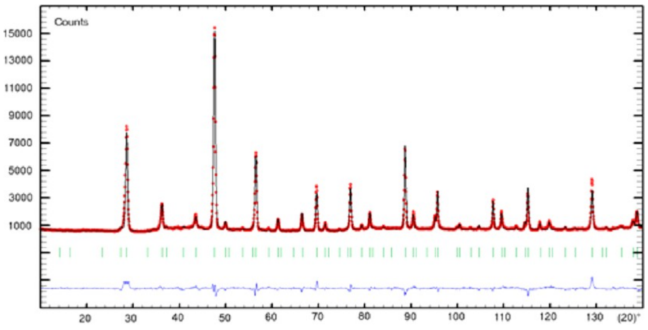

Figure 13. Refined diffraction pattern from neutron data for $La_{10}W_2O_{21}$. Red dots represent the observed data, the black line represents the calculated ones, Bragg ticks are the peak positions, and the blue curve shows the difference between the observed and calculated patterns. λ = 1.596125 Å.

disorder evidenced pushes us to explore the ionic conductivity of the compound. A single-crystal pellet was also tested.

The Nyquist plot of the measurement presents a typical Warburg behavior for the low-frequency range (Figure 16) usually associated with pure ionic conductors. On the Arrhenius plot the $La_{10}W_2O_{21}$ compound presents a modest ionic conductivity in comparison with $La_2Mo_2O_9$ or YSZ. The activation energy is comparable with other good oxide ion conductors. We have tested the reproducibility of those conductivity values performing the same measurement at 9 months interval (Figure 17a), and we have tested different types of samples. As shown in the Arrhenius plot, the sample did not evolve in time. We also notice a difference between powder pellet and single-crystal pellet (Figure 17b) due certainly to the presence of grain boundaries in the former.

Two behaviors can be observed depending on frequencies: the first corresponding to the bulk and the second to the boundaries. The total conductivity of the sample has been obtained from equivalent electrical circuit and a fit with ZView.[59] The Arrhenius plot of the ac $La_{10}W_2O_{21}$ conductivity is shown on Figure 17b, compared with LAMOX. The evolution is close to linear, and the related activation energy is found at E_a = 0.54 eV.

A thermogravimetric analysis under N_2–H_2 (5%) was also performed at various temperatures (500, 600, and 700 °C) during one night to analyze the stability under reduced atmosphere. Any mass change arises.

The question of the conduction mechanism is now open; a structural analysis in a previous part shown through a simulation of ionic pathway gives a clue.

The volume expansion was measured in the range of 25–1150 °C by high-temperature X-ray diffraction. We calculate an expansion coefficient of $\alpha_{25,1150} = 12.2 \times 10^{-6}$ °C^{-1} This result is comparable with the result obtained from La_2WO_6, $\alpha_{30,1000} = 11.6 \times 10^{-6}$ °C^{-1},[60] studied previously; it takes place in a classical oxide volume expansion value.

Table 4. Experimental and Synchrotron/Neutron Combined Rietveld Refinement Details for $(La_{5.667}W_{0.333})LaWO_{14}\square_2$ (Corresponding to $La_{10}W_2O_{21}$)

symmetry	cubic	cubic
space group	$F\bar{4}3m$	$F\bar{4}3m$
cell param, *a* (Å)	11.17932(6)	11.17932(6)
Z	4	4
vol (Å^3)	1397.16(2)	1397.16(2)
radiation	synchrotron	neutron
diffractometer	BM01A, ESRF	D2B, ILL
wavelenght (Å)	0.60044	1.59613
pattern range (2θ, deg)	4.20–50.80	10.00–141.40
step size (2θ, deg)	0.003	0.05
temp (K)	293	293
No of contributing reflns	143	89
No of refined params (total)	104	104
No of atomic coordinate params	5	5
No of thermal params	13	13
No of background params	30	29
pseudo-Voigt profile shape, *h*	0.34(1)	0.28(3)
Half-Width Parameters		
U	0.0096(2)	0.104(5)
V	0	−0.28(1)
W	0.00033(1)	0.308(6)
Conventional Rietveld Reliability Factors (%)		
R_P	13.8	16.9
R_{WP}	13.3	14.9
R_{exp}	7.41	5.23
R_B	4.71	8.60
R_F	4.36	7.91

DISCUSSION OF RECENT WORKS

Magraso et al. have obtained more or less similar crystallographic and conductivity results by using a freeze-drying wet-chemical synthesis route. A major difference must be underlined: the La/W ratio, which they found at 5.6, in our study is 5. This fact could be easily explained by the role played by the synthesis route.

Solid-state and wet-chemical synthesis routes need totally different reactivity schemes, implying two distinct thermodynamic pathways. Moreover, as shown in the La_2O_3–WO_3 Yoshimura phase diagram, at higher temperature "$La_{10}W_2O_{21}$" presents a solid solution, pointing to the possibility of varying La/W ratio within a given structure. All of this information seems to be in agreement with the cell parameter's evolution dependence as a function of the La/W ratio (from 11.173 to 11.188 Å).

Finally, Haugsrud et al.,[22] Magraso et al.,[23] Lashtabeg et al.,[61] and our conductivity results are similar. Indeed, we think that a proton conductivity from $La(OH)_3$ impurity could play a role. At this point, Haugsrud et al.'s phase identification seems rather surprising since it is not possible to obtain La_6WO_{12} at temperatures lower than 1700 °C.

CONCLUSION

The $La_{10}W_2O_{21}$ structure has been elucidated in an ab initio way from CBED, synchrotron and neutron powder diffraction data. The initial formula has been reformulated to $La_{14}W_2O_{27}$

Table 5. Crystallographic Parameters of $La_{10}W_2O_{21}$ Obtained from Synchrotron−Neutron Mixed Rietveld Refinement

atom	position	occupancy	x	y	z	U_{11}	U_{22}	U_{33}	U_{12}	U_{13}	U_{23}	U_{iso}
La1/W1	24g	0.94/0.06	0.0005(4)	1/4	1/4	0.0100(7)	0.0430(5)	$=U_{22}$	0	0	−0.0313(6)	0.0320(6)
La2	4a	1	0	0	0	0.0179(6)	$=U_{11}$	$=U_{11}$	0	0	0	0.0179(6)
W2	4b	1	1/2	1/2	1/2	0.0055(4)	$=U_{11}$	$=U_{11}$	0	0	0	0.0055(4)
O1	16e	1	0.8660(4)	$=x$	$=x$	0.021(2)	$=U_{11}$	$=U_{11}$	−0.006(2)	$=U_{12}$	$=U_{12}$	0.021(2)
O2	16e	1	0.1291(7)	$=x$	$=x$	0.038(3)	$=U_{11}$	$=U_{11}$	−0.005(2)	$=U_{12}$	$=U_{12}$	0.038(3)
O3	16e	1	0.4032(7)	$=x$	$=x$	0.093(4)	$=U_{11}$	$=U_{11}$	−0.040(3)	$=U_{12}$	$=U_{12}$	0.093(4)
O4	16e	0.5	0.611(2)	$=x$	$=x$	0.16(3)	$=U_{11}$	$=U_{11}$	−0.020(18)	$=U_{12}$	$=U_{12}$	0.16(3)

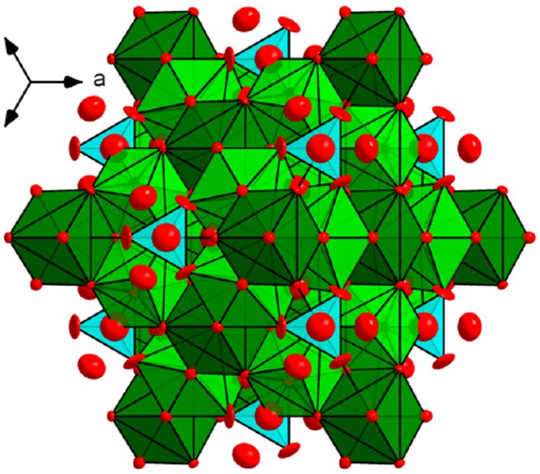

Figure 14. Unit cell projection of the $La_{10}W_2O_{21}$ structure along the [111] direction. Ellipsoids are represented at 50% probability, the largest corresponding to the O4 sites (half-occupied).

Table 6. Selected Bond Distances (Å) for $La_{10}W_2O_{21}$

La1−O1	×2	2.372(5)	La2−O1	×4	2.595(4)
La1−O2	×2	2.392(8)	La2−O2	×4	2.500(8)
La1−O3	×2	2.651(8)	W2−O3	× 4	1.874(8)
La1−O4		2.53(2)	W2−O4[a]	×2	2.15(2)

[a] O_4 half-occupied.

following the powder structure determination with direct space methods. We analyzed and discussed at length the pyrochlore distortions, and a clear distinction has been established between "La_6WO_{12}" and "$La_{10}W_2O_{21}$".

The compound crystallizes within the cubic space group $F\overline{4}3m$ (a = 11.17932(6) Å). The structure is built from classically two lanthanum polyhedra in 7- and 8-fold coordination and from one unexpected La−W mixed crystallographic position. This La−W mixed crystallographic position has been nicely confirmed by ^{139}La NMR. This structure moreover presents disorder and twinning.

Another property highlighted by comparison with Magraso's work, is the dependence of the stability domain upon the chemical synthesis route.

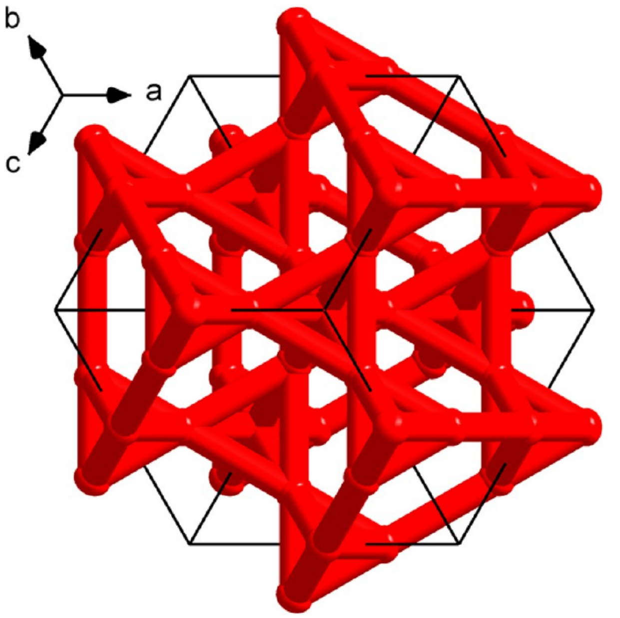

Figure 15. Hypothesis for the conduction by the oxygen atom O4 (half-occupied site), by jump to the next vacancies.

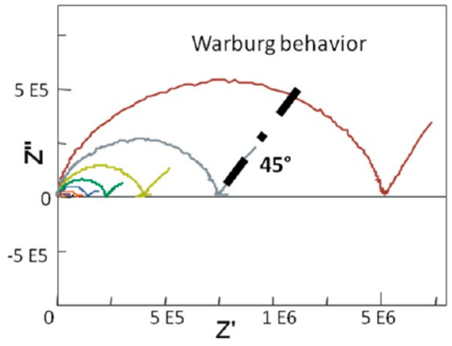

Figure 16. Alternating current impedance plot of $La_{10}W_2O_{21}$ at various temperatures (where, for example, 5 E5 represents 5 × 10^5). The Warburg behavior at low frequencies is underlined.

This definite compound exhibits an interesting conductivity easily explained by the structure which presents ionic paths,

Table 7. Calculated Bond Valence for $La_{10}W_2O_{21}$ Neglecting the W Substitution on La1

	O1	O2	O3	O4[a]	Σ
La1	0.582 × 2 × 3	0.552 × 2 × 3	0.274 × 2 × 3	0.380 × 3	3.20
La2	0.319 × 2 × 1	0.412 × 4 × 1			2.92
W2			1.123 × 4 × 1	0.533 × 2 × 1	5.56
Σ	2.06	2.07	1.95	1.67	

[a] O_4 half-occupied.

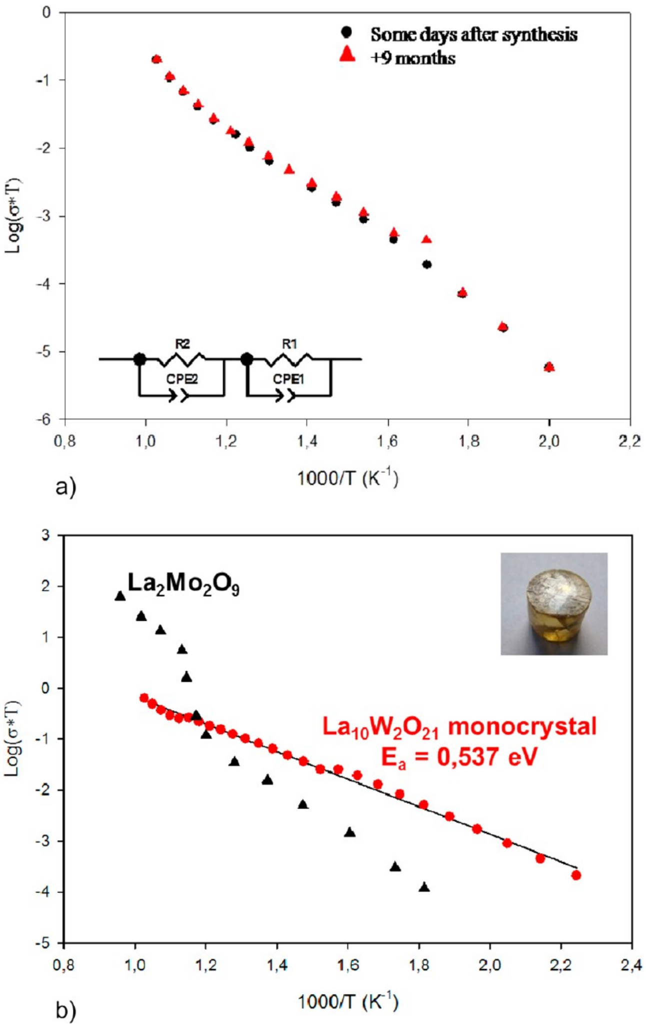

Figure 17. Arrhenius plots of $La_{10}W_2O_{21}$ on a powder pellet (a) and on a single crystal pellet (b). There is a comparison in 9 months of distance, between Arrhenius behavior of the same powder pellet (a). In panel b, $La_{10}W_2O_{21}$ Arrhenius behavior is compared to $La_2Mo_2O_9$. The equivalent circuit used is shown in the inset of panel a.

with reasonably low activation energy, by jumping to the next vacancies due to disorder on the 24g Wyckoff position.

■ ASSOCIATED CONTENT

Ⓢ Supporting Information

Crystallographic parameters obtained from refinement of mixed synchrotron and neutron powder diffraction data. This material is available free of charge via the Internet at http://pubs.acs.org.

■ AUTHOR INFORMATION

Corresponding Author

*E-mail: mh_chambrier@yahoo.fr.

Notes

The authors declare no competing financial interest.

■ ACKNOWLEDGMENTS

We acknowledge Dr. Wouter Van Beek for his great availability during synchrotron (E.S.R.F. Grenoble) and neutron (I.L.L Grenoble) experiences and the support of “Très Grands Instruments de Recherche” for ^{139}La NMR experiences.

■ REFERENCES

(1) Lacorre, P.; Goutenoire, F.; Bohnke, O.; Retoux, R.; Laligant, Y. *Nature* **2000**, *404*, 856−858.

(2) : Subbarao, E. C. In *Science and Technology of Zirconia I*, Advances in Ceramics, Vol. 3; Heuer, A. H., Hobbs, L. W., Eds.; American Ceramic Society: Columbus, OH, USA, 1981; pp 1−24.

(3) Harwig, H.; Gerards, A. G. *J. Solid State Chem.* **1978**, *26*, 265−274.

(4) Esaka, T.; Minaai, T. A.; Iwahara, H. *Solid State Ionics* **1992**, *57*, 319−325.

(5) Huang, K. Q.; Tichy, R. S.; Goodenough, J. B. *J. Am. Ceram. Soc.* **1998**, *81*, 2565−2575.

(6) Ishihara, T.; Matsuda, H.; Takita, Y. *J. Am. Chem. Soc.* **1994**, *116*, 3801−3803.

(7) Berastegui, P.; Hull, S.; Garcia-Garcia, F. J.; Eriksson, S. G. *J. Solid State Chem.* **2002**, *164*, 119−130.

(8) Abraham, F.; Debreuille-Gresse, M. F.; Mairesse, G.; Nowogrocki, G. *Solid State Ionics* **1988**, *28−30*, 529−532.

(9) Kramer, S. A.; Tuller, H. L. *Solid State Ionics* **1995**, *82*, 15−23.

(10) Guillot, S.; Beaudet-Savignat, S.; Lambert, S.; Roussel, P.; Tricot, G.; Vannier, R. N.; Rubbens, A. *J. Raman Spectrosc.* **2011**, *42* (6), 1455−1461.

(11) West, A., *Solid State Chemistry and Its Applications*; John Wiley & Sons: New York, 1985.

(12) Kharlamova, T.; Pavlova, S.; Sadykov, V. A.; Krieger, T.; Batuev, L.; Muzykantov, V.; Lapina, O.; Khabibulin, D.; Chaikina, M.; Uvarov, N.; Pavlukhin, Y.; Petrov, S.; Argirusis, C. *MRS Proc.* **2008**, *1126*, No. 1126-S11-04.

(13) Shannon, R. D. *Acta Crystallogr.* **1976**, *A32*, 751−767.

(14) Yoshimura, M.; Rouanet, A. *Mater. Res. Bull.* **1976**, *11* (2), 151−158.

(15) Czeskleba-Kerner, H.; Cros, B.; Tourne, G. *J. Solid State Chem.* **1981**, *37* (3), 294−301.

(16) Tkachenko, E. A.; Fedorov, P. P. *Inorg. Mater.* **2003**, *39* (Suppl.1), 25−45.

(17) Bevan, D. J. M.; Drennan, J. *Acta Crystallogr.* **1982**, *B38*, 2991−2997.

(18) Wyckoff, R. W. G., *Crystal Structures*, 2nd ed.; Interscience Publishers: New York, 1960; p 439.

(19) Subramanian, M. A.; Aravamudan, G.; Subba Rao, G. V. *Prog. Solid State Chem.* **1983**, *15*, 55−143.

(20) Luan, J.-F.; Hao, X.-P.; Zheng, S.-R.; Luan, G.-Y.; Wu, X.-S. *J. Mater. Sci.* **2006**, *41*, 8001−801.

(21) Zhou, Q.; Kennedy, B. J.; Ting, V.; Withers, R. L. *J. Solid State Chem.* **2005**, *178*, 1575−1579.

(22) Haugsrud, R.; Kjolseth, C. *J. Phys. Chem. Solids* **2008**, *69* (7), 1758−1765.

(23) Magraso, A.; Frontera, C.; Marrero-Lopez, D.; Nunez, P. *Dalton Trans.* **2009**, 10273−10283.

(24) Massiot, D.; Farnan, I.; Gautier, N.; Trumeau, D.; Trokiner, A.; Coutures, J.-P. *Solid State Nucl. Magn. Reson.* **1995**, *4*, 241−248.

(25) Tong, Y. Y. *J. Magn. Reson., Ser. A* **1996**, *119*, 22−28.

(26) Fayon, F.; Landron, C.; Sakurai, K.; Bessada, C.; Massiot, D. *J. Non-Cryst. Solids* **1999**, *243*, 39−44.

(27) Massiot, D.; Fayon, F.; Capron, M.; King, I.; Le Calve, S.; Alonso, B.; Durand, J. O.; Bujoli, B.; Gan, Z.; Hoatson, G. *Magn. Reson. Chem.* **2002**, *40*, 70.

(28) Solartron Materials Research and test software, (2004).

(29) Yoshimura, M.; Sibieude, F.; Rouanet, A.; Foex, M.. *J. Solid State Chem.* **1976**, *16*, 219−232.

(30) Ismunandar; Kennedy, B. J.; Hunter, B. A.; Vogt, T. *J. Solid State Chem.* **1997**, *131*, 317−325.

(31) Fender, B. E. F.; Willis, B. T. M. *Chemical applications of thermal neutron scattering*; Oxford University Press: London, 1974; pp 250−270.

(32) Vannier, R. N.; Abraham, F.; Nowogrocki, G.; Mairesse, G. J. *J. Solid State Chem.* **1999**, *142*, 294−304.

(33) Thompson, A. R.; Oldfield, E. *J. Chem. Soc., Chem. Commun.* **1987**, 27−29.

(34) Dupree, R.; Lewis, M. H.; Smith, M. E. *J. Am. Chem. Soc.* **1989**, *111*, 5125−5132.
(35) Bastow, T. J. *Solid State Nucl. Magn. Reson.* **1994**, *3*, 17−22.
(36) Hunger, M.; Engelhardt, G.; Weitkamp, J. *Microporous Mater.* **1995**, *3*, 497−510.
(37) Bastow, T. J.; Mathews, T.; Sellar, J. R. *Solid State Ionics* **2004**, *175*, 129−133.
(38) Czjzek, G.; Fink, J.; Götz, F.; Schmidt, H.; Coey, J. M. D.; Rebouillat, J. P. *Phys. Rev. B: Condens. Matter Mater. Phys.* **1981**, *23*, 2513−2530.
(39) Le Caër, G.; Brand, R. A. *J. Phys.: Condens. Matter* **1998**, *10*, 10715−10774.
(40) Massiot, D.; Fayon, F.; Capron, M.; King, I.; Le Calvé, S.; Alonso, B.; Durand, J. O.; Bujoli, B.; Gan, Z.; Hoatson, G. *Magn. Reson. Chem.* **2002**, *40*, 70−76.
(41) Le Caër, G.; Bureau, B.; Massiot, D. *J. Phys.: Condens. Matter* **2010**, *22*, No. 065402.
(42) Rodriguez-Carvajal, J. Abstracts of the Satellite Meeting on Powder Diffraction. *XV Congress of the IUCr*, Toulouse, France; International Union of Crystallography: Chester, England, 1990; p 127.
(43) *ISOTROPY Software Suite*, iso.byu.edu
(44) Gonzales-Platas, J. ; Rodriguez-Carvajal, J. *Graphic Fourier Programme GFOURIER*, v. 3,2; Laboratoire Léon Brillouin: Saclay, France, 2003.
(45) Buxton, B. F.; Eades, J. A.; Steeds, J. W.; Rackham, G. M. *Proc. R. Soc. London* **1976**, *A281*, 171.
(46) Tanaka, M.; Saito, R.; Sekii, H. *Acta Crystallogr., Sect. A: Found. Crystallogr.* **1983**, *39*, 357−368.
(47) Morniroli, J. P.; Steeds, J. W. *Ultramicroscopy* **1992**, *45*, 219−239.
(48) Redjaïmia, A.; Morniroli, J. P. *Ultramicroscopy* **1994**, *53*, 305−317.
(49) *International Tables for Crystallography*; Hahn, T., Ed.; Reidel: Dordrecht, The Netherlands, 1988.
(50) Werner, P.-E. *Z. Krist.* **1964**, *120*, 375−387.
(51) Boultif, A.; Louër, D. *J. Appl. Cryst.* **2004**, *37*, 724−731.
(52) Le Bail, A. *Powder Diffr.* **2004**, *19*, 249−254.
(53) Le Bail, A. *Powder Diffr.* **2005**, *20*, 316−326.
(54) Rodriguez-Carvajal, J. *Physica B* **1993**, *192*, 55−69.
(55) Le Bail, A. *Mater. Sci. Forum* **2001**, *378*−*381*, 65−70.
(56) Ehrenberg, H.; Hartmann, T.; Bramnik, K. G.; Miehe, G.; Fuess, H. *Solid State Sci.* **2004**, *6*, 247−250.
(57) Chambrier, M.-H.; Le Bail, A.; Kodjikian, S.; Suard, E.; Goutenoire, F. *Inorg. Chem.* **2009**, *48*, 6566−6572.
(58) Marrero-Lopez, M.; Pena-Martinez, J.; Ruiz Morales, J. C.; Nunez, P. *J. Solid State Chem.* **2008**, *181*, 253−262.
(59) Johnson, D. *ZView*, version 2.9b; Scribner Associates: Southern Pines, NC, USA.
(60) Chambrier, M. H.; Kodjikian, S.; Ibberson, R. M.; Goutenoire, F. *J. Solid State Chem.* **2009**, *182*, 209−214.
(61) Lashtabeg, A.; Bradley, J.; Dicks, A.; Auchterlonie, G.; Drennan, J. *J. Solid State Chem.* **2010**, *183*, 1095−1101.